Title

Coupling dynamic in situ X-ray micro-imaging and indentation: A novel approach to evaluate micromechanics applied to oil shale

Authors
Voltolini, Marco
Rutqvist, Jonny
Kneafsey, Timothy

Publication Date
2021-09-01

DOI
10.1016/j.fuel.2021.120987

Peer reviewed

Coupling Dynamic In Situ X-Ray Micro-Imaging And Indentation: A Novel Approach To Evaluate Micromechanics Applied To Oil Shale

Marco Voltolini[1], Jonny Rutqvist[1], and Timothy Kneafsey[1]

[1] Energy Geosciences Division, Lawrence Berkeley National Laboratory. 1 Cyclotron Road, Berkeley, CA 94720.

Abstract

Oil and gas shales are a system where understanding the mechanical properties at the microscale is of paramount importance, e.g. to better understand the behavior of proppant-shale contacts and their role in the evolution of propped fractures in unconventional reservoirs. This work shows for the first time an experiment coupling indentation testing with in situ X-ray imaging in a Green River shale sample. A full compliance curve has been measured with the sample in water, allowing to visualize the indentation of the sample in function of axial load, in a purpose-built system for combined in situ indentation and X-ray imaging. A series of 3D datasets were used for a digital volume correlation study to obtain local strain fields. This analysis has been complemented with the analysis of cracks. Finally, geomechanical modeling has been carried out to replicate and generalize the observed behavior in the shale. This study validated this experimental approach, providing a breakthrough in understanding micro-mechanics in shales, and demonstrates how this class of experiments can be important for studies involving the prediction of the evolution of propped fractures in shale reservoirs, with possible applications in a much larger number of application fields (geothermal, materials science, etc.)

Keywords: Green River Shale, ductile shale, X-ray micro-tomography, Micro-mechanics, Brinell-type indentation, Geomechanical modeling, proppant embedment.

1. Introduction

Tight oil and gas shale exploitation has been a revolution that redesigned the map of the global players in fossil energy production (Knaus et al., 2010; Hart et al., 2011; Chengzao et al., 2012). This change has been made possible by the constant improvements in the field of horizontal drilling techniques, coupled with hydraulic fracturing of the source rock through the injection of pressurized fluids used to increase the effective permeability of the source rock, typically characterized by low intrinsic permeability. Fractures generated by the injection of the pressurized fluids tend to close because of the overburden pressure, once pressurization stops. To avoid this issue, proppant grains, included in the injection fluid, are placed in the fractures to mechanically contrast their closure (e.g. Liang et al., 2016).

The usable fracture life in oil and gas shale wells is rather unpredictable: many factors are at play simultaneously and they all can affect the closure rate of propped fractures. Among these factors, the mechanical properties of proppant grains and shale have a mayor impact, these properties can also be significantly impacted by surface modifications, due to chemically aggressive fracturing fluids inducing dissolution or scaling (Li et al., 2019), for example. All these problems have in common that the main controlling factor (especially when considering the ideal case of a fracture filled with a proppant monolayer) of the fracture closure is the proppant-shale mechanical interaction at the contacts: depending on the stress, temperature, mineralogy, and fabric of the shale at the contacts, we could observe proppant shattering, proppant embedding in a ductile fashion, proppant embedding in a brittle fashion, etc. and each of these processes has an impact on fracture properties such as conductivity (Voltolini and Ajo-Franklin 2020). Being able to understand and predict these *micro*scale behaviors is key for understanding properties of the propped fractures at the *macro*scale. More accurate predictive tools in this field can have a significant impact on tight oil and gas exploitation, for example helping to design better procedures requiring less fracturing/refracturing events (decreased use of water, mitigated risk of induced seismicity), and to evaluate risks connected to the usage of chemicals (e.g. the impact of injection of acids during the shut-in period: how does the chemical weathering of the surface impacts proppant embedment?).

Micro- and nano- indentation measurements are used, among other techniques, to assess the mechanical properties of materials on a surface (e.g. Liu et al., 2016; Yang et al., 2016), which is used to infer the general "fracability" of a shale, when coupled with other measurements. Conventional indentation measurements are subject to two main limitations: i) in the subsurface the fracture is at non-ambient conditions (e.g. presence of a specific fluid, temperature, etc.), ii) it is not possible to understand the *local* deformation in the sample, under and around the indenter tip. To overcome these limitations, we have developed and tested a novel experimental approach coupling in situ synchrotron X-ray imaging and indentation, using a mini-triaxial cell developed for synchrotron X-ray micro-computed tomography (SXRμCT) (Voltolini et al., 2017) as an indenter device. The work performed is an extension of the concept first applied on foamed plaster by Bouterf et al., (2014). The cell itself allows working at non-ambient conditions (fluids, pressurization, temperature, etc.) and collecting 3D imaging datasets during the indentation process. Image processing techniques, such as digital volume correlation, can provide quantitative information about the deformation field *inside* the sample and the microfracturing along the measured compliance curve. We propose this approach to utilize this unprecedented amount of information describing the mechanical response of an oil shale during indentation to validate mathematical models aiming at generalize these behaviors, and to better understand controlling factors and important input parameters required. The long-term goal is to build predictive models that can be used to better evaluate hydraulic fracturing scenarios and helping with proper exploitation strategies avoiding unnecessary use of water resources and hazardous chemicals, and decrease the need of re-fracturing events. This can be obtained with a better evaluation of the usable life of a propped fracture in a given system by estimating the behavior of proppant (embedment, shattering, etc.). Understanding the micromechanical response is also important to evaluate whether the aggressive chemicals used in the shut-in period weaken the fracture surface in a way that enhances proppant embedment (thus potentially shortening the usable life of the well). Finally, the new techniques that target the controlled modification of the fracture surfaces in ductile shales by making them mechanically stronger, now being developed to enable the exploitation of oil shales rich in clays and/or organics (displaying a markedly ductile behavior, especially at high temperatures), can be directly tested at relevant reservoir conditions.

2. Materials and Methods

2.1 Sample characterization

The sample used in this study is an immature Green River shale sample collected in the Uinta Basin in Colorado belonging to the PR-15-3C core (Box #9, 77 ft.). The sample is a fine grained-shale, almost black in color, and with visible fine banding, with a substantial amount of organic material: the Fischer assay in the same section of the rock gave a 41.6 gal/ton (157.5 liters/ton) of recovery. To characterize the mineralogy of the sample, we measured an X-ray powder diffraction profile and run a Rietveld analysis (Chateigner, 2013) to obtain phase fractions (profile and fit are provided in the Supplementary Material SM1). Results, as summarized in Table 1, highlight the presence of substantial dolomite, and the only clay phase present is illite. From the mineralogical analysis alone, the composition would suggest high stiffness and a rather brittle behavior (lithics = 42.3%, carbonates = 47.2%, clays = 10.5%), not too dissimilar from the shales analyzed in Voltolini et al., (2020). The high amount of organic material in this sample is not only inferred from the Fischer assay results: the X-ray diffraction profile also shows an evident modulation of the background of the profile, hinting at a substantial presence of amorphous material, which in the present case is the organic matter. The presence of this organic fraction will have a substantial impact on the mechanical properties of this sample. This impact in propped fractures, and its dependence on temperature, has been studied in Voltolini (2020).

2.2 The combined X-ray imaging and indentation apparatus

In order to run the experiment shown in this work, we have adapted the mini-triaxial cell used for SXRμCT described in detail in Voltolini et al., (2017). This specific cell allows to set a pore pressure, a confining pressure, and an axial pressure, constant flow, and -to some extent- controlled temperature up to ~50 °C. This system was adapted by mounting the shale sample, a cylinder 7.1 mm in diameter and 6.1 mm in height, in an aluminum (6061 alloy) sleeve of 1 mm of thickness. To avoid confinement issues, the thin gap (~0.2 mm, on average) between sample and sleeve was filled with epoxy resin. The resin was not thin enough to penetrate in the sample and altering its structure. The sample was flattened at both ends using diamond-plated disks, and placed directly onto the lower piston of the triaxial cell. On the upper piston, a nonporous alumina (for stiffness) cylinder 9.5 mm in diameter and ~ 2 cm in height was connected. On the lower face of the piston, a Silicon nitride ball 2.38 mm in diameter was glued in place in a small rounded recess on the face, to aid keeping it in place and in contact with a larger area of alumina (to avoid indentation on the supporting structure). The spherical shape of the indenter (Brinell-type) was chosen because of both its ease of implementation and because it can be considered as an "ideal proppant grain", extremely stiff, hard, and perfectly spherical, making the transition from indentation test and model to the field interpretation easier. Another factor to consider is the size larger than the typical micro-indenter tip. Preliminary tests have been run with smaller spheres (and higher imaging resolution as well), but this size proved to be better for different reasons: i) it is the ideal size for this kind of measurements in terms of field of view, resolution and energy available at the synchrotron beamline. ii) It increased the precision of the load-indentation curve since larger force increments are needed to indent the sample, reducing uncertainties and factors such as gasket friction. iii) The indentation averages over a slightly larger (compared to conventional micro-indenters) area, thus giving a more meaningful result for the whole shale (since multiple measurements on the same sample are not feasible). The whole sample/piston assembly was mounted into a PVDF sleeve to keep all the parts in place and to isolate the sample from the confining medium. The sleeve was sealed with gapless pinch clamps to secure the separation of confining medium and the pore fluid. The lateral confining space was connected to a dedicated Teledyne ISCO pump (260HP) to provide lateral confining pressure (in this experiment was kept extremely low just to ensure proper contact of the outer sleeve), and another pump was connected to the axial ram on the top of the cell to provide the vertical load. The axial system was calibrated to be able to directly convert the pressure set in the pump (working at constant pressure mode, between the manual increase/decrease steps used to measure the indentation curve) to kilogram-force applied on the sample.

2.3 Imaging measurement experimental setup

The experiment was run at the 8.3.2. beamline at the Advanced Light Source at the Lawrence Berkeley National Laboratory (MacDowell et al., 2012). The radiation used for the experiments was filter-hardened white light from the superbending magnet source of 8.3.2., with 6 mm of Aluminum and 0.5 mm of copper filters to preferentially cut the low energy portion of the spectrum. The detector system consisted in a 50 μm thick Ce:LuAG followed by a 2× optical lens system, providing a pixel size of 3.22 μm and a resulting lateral field of view of 8.24 mm. Exposure time was 260 ms per projection and 1312 projections over a 180 degrees rotation were collected for tomographic imaging. The resulting dataset was 2560 × 2560 × 1560 px^3. The same setup and exposure time were used also for the collection of radiographs during the fine load increment between tomographic measurements. Radiographs were subject to a conventional flat-field correction and normalization, and tomographic datasets were reconstructed using a filtered back-projection algorithm as included in the "Octopus" software (Dierick et al., 2004); the resulting stack of slices was combined to obtain volumes with the Fiji software (Schindelin et al., 2012) that was also used for the data handling.

2.4 Indentation measurement

The cell was assembled to ideally keep the sample at water-saturated conditions. The sample was kept in water for ~5 hours before the cell assembly, and the sample chamber was in water during the whole experiment. A 50 psi (0.34 MPa) confining pressure was applied just to keep the sleeve in contact with the assembly. Axial pressure was increased in 25 psi steps (equivalent to a ~1.7 kgf increase of axial load per step). At each step the system was let stabilize for ~10 minutes before taking the radiographs, used to calculate the indentation curve. In the unloading curve the data were collected in steps of 100 psi. A total of 64 steps were collected to build the compliance curve from the measurements on the radiographs. The compliance curve was obtained by measuring directly on the radiographs the indentation diameter (and therefore the indentation depth) for each loading step. Every 200 psi, or when potentially significant changes/events were observed during the experiment, an additional tomographic dataset was also collected to measure the local deformation *in* the sample.

2.5 Quantitative image processin

Volumes were cropped and rotated in order to have a clean sample and the bedding in the horizontal direction when looking at the single slices. Two main image analysis techniques were used on these datasets: 1) Digital volume correlation (DVC) to measure the local displacements of the sample during the indentation, and 2) Crack aperture analysis, to measure the evolution of the cracks in the sample.

DVC analysis is based on the calculation of the correlation of patterns found in subvolumes in a pair of tomographic datasets of the same sample at different deformation stages, this allows for the calculation of a 3D map of the local displacements, typically resulting in three volumes with the displacements along the Cartesian directions for each subvolume. For the DVC analysis we rescaled the volumes to 418 px × 418 px × 295 px, used a isotropic correlation window of 7 px with a node spacing of 4 px. A total of 7 DVC analyses (the loading section of the curve) run on the software TomoWarp2 (Tudisco et al., 2017) are presented in the results; the average correlation coefficient in the shale was 0.9993, highlighting the reliability of the correlation process.

The analysis of the development of the crack around the indenter tip was carried out in Fiji by cropping the volume where the crack, subparallel to the bedding, was present. Subsequently, the crack aperture maps were calculated by measuring the thickness of the crack, pixel-by-pixel, in the direction orthogonal to the crack surface.

2.6 Modeling the indentation process

The numerical modeling of this experiment is part of an ongoing effort to improve the coupled multiphase fluid flow and geomechanical modeling of proppant-filled fractures during hydrocarbon production. The necessary model developments and applications are based on the linking of the TOUGH2 multiphase flow simulator with the FLAC3D geomechanical simulator (Rutqvist, 2017). While the simulator has been extensively applied for modeling of coupled processes in shale for various applications related to geologic carbon sequestration, nuclear waste disposal, and shale gas fracturing (Rutqvist and Tsang, 2002; Rutqvist et al., 2014; Rutqvist et al., 2015), it is here for the first time applied for micromechanical modeling. The modeling of the indentation tests involves non-linear elasto-plastic and anisotropic material behavior under large deformation. The materials are represented in FLAC3D by polyhedral elements that behaves according to a prescribed linear or nonlinear stress/strain law in response to applied forces or boundary restraints. The material can yield and flow, and the grid can deform (in large-strain mode) and move with the material as will be required for modeling significant proppant embedment into the shale sample. The explicit, Lagrangian calculation scheme and the mixed-discretization zoning technique used in FLAC3D ensure that plastic collapse and flow are modeled very accurately (Itasca, 2011).

The modeling domain has to be discretized with a dense mesh to capture the expansion of yielding and brittle fracture initiation and propagation. The shale anisotropic material is modeled using a so-called ubiquitous joint model consisting of matrix strength properties and properties along weak planes that are parallel with shale bedding (Itasca, 2011). A Mohr-Coulomb model with tensile cut-off is used considering shear and tensile failure, both in the matrix and along weak planes. More brittle or ductile mechanical behavior can be modeled by strain softening or hardening of shear strength parameters (cohesion and friction angle) and tensile strength. The modeling further requires accurate simulations the contact friction between the Silicon nitride indenter and the shale surface. The interface between the Brinell indenter and the shale considers interface properties, including cohesion and coefficient of friction in a Coulomb model (Itasca, 2011).

3. Results and Discussion

The analyses carried out were aiming at understanding the mechanical response of the shale by coupling mechanical and morphological/textural data. The focus was to obtain a loading/unloading curve of a Brinell-type indentation measurements, and evaluate in a quantitative fashion the local deformation of the sample and to better understand the micromechanical properties of this shale in general.

3.1 The compliance curve

The full loading/unloading curve has been calculated from the images and it is plotted in Fig. 1a: the shape of the curve is compatible with a Brinell-type indentation of a material with a partially ductile behavior. The shape of the very first part of the loading curve is due to the sample arrangement in the experimental setup and the friction of the upper piston with the seals of the confining pressure setup. Through a series of tests (friction measurements on the upper piston, load sensor at the sample position) it has been estimated that values below ~6 kgf (less in case of loose sealing of the piston, ~3 kgf, when limited low or no confining pressure is used) in the very first stage of loading are not reliable, due to these problems. The values obtained from the radiographs have also been used to calculate the pressure on the indenter contact surface (Fig. 1b), which is the equivalent of the "Meyer hardness" values. Meyer hardness H for a Brinell indenter is defined as follows:

$$H = \frac{P}{A} = \frac{4P}{\pi d^2}$$

where P is the total pressure, A the area of the indent, and d the diameter of the indentation (Fischer-Cripps, 2011).

In order to measure the Young's modulus of the sample, the analysis of the slope of the unloading curve at maximum load was carried out. The upper part of the curve at maximum load was used, to average the behavior from oscillations and uncertainties encountered in using the only 2-3 points closer to the higher load, and first the reduced Young's modulus E^* was calculated as:

$$E^* = \frac{1}{2}\frac{\sqrt{\pi}}{\sqrt{A}}\frac{dP}{dh}$$

where h is the depth of the indentation. This resulted in E^* = 7.92 GPa. Considering the Poisson's ratio for this type of shales found in literature, ν = 0.35 (Eseme et al., 2007), the Young's modulus can be calculated as:

$$E = E^{*}(1 - \nu^{2})$$

resulting in E = 5.95 GPa, a value in very good accordance with bulk measurements run on Green River samples with similar grade obtained via Fischer assay (Agapito and Hardy, 1982; Eseme et al., 2007).

The measurement of a loading/unloading curve using X-ray images to calculate the indentation depth, at in situ conditions, presents some limitations when compared to the conventional micro-indentation systems: the precision is significantly lower because it is not a single-purpose dedicated instrument with a high-precision load sensor, the measurement requires a set up with several complications incompatible with precise force measurements (e.g. gaskets, as previously mentioned), and experiments require a much longer time. Conventional micro-indentation is a much easier and faster process, thus allowing multiple measurements on a single surface of the sample in a short amount of time. On the other hand, the system presented in this work has some significant advantages: first, the environment can be controlled over a number of variables. As a first test for this concept/technique, we ran the measurement with the sample in water, at room temperature and atmospheric pore fluid pressure, to be able to better evaluate what kind of results can be reasonably achieved and the critical parts of the instrument needing upgrades. The current setups available can be utilized to run indentation + imaging experiments at much more extreme conditions. For example we could use pressurized fluid by controlling pore pressure and confining pressure in the cell. Another possibility would be to run indentation + imaging experiments at both high pressure and temperature, using a cell as the one described in Voltolini et al., (2019). This would be extremely useful for materials in general, but for oil shales in particular, since their mechanical behavior can be extremely different at reservoir temperature and pressure when compared to room temperature and pressure: for example an organics-rich shale subject to pyrolysis at room pressure develops a system of microcracks (Tiwari et al., 2013;

Saif et al., 2017), whereas at high pressure it behaves in a ductile fashion (Voltolini et al., 2019), making realistic in situ experiment essential to better understand the behavior of shales in the subsurface. Conventional micro-indentation tests, albeit being extremely useful to understand the generic micro-mechanics of the sample, cannot address these important problems; where the tests performed in air in the lab cannot be easily translated to the behavior at the relevant pressure, temperature, and chemical conditions. In this scenario, the approach we used here demonstrates, with its intrinsic limitations, that it could be employed in those cases successfully. Future development of cells more specifically dedicated to this class of measurements could improve the measurement precision, ease of setup, and add some new, compatible, features such e.g. viscosity measurements at high temperature and pressure, by using different probes.

Nevertheless, the ability to perform "simple" indentation measurements at non-ambient conditions is only a part of the advantages of the approach we are presenting in this work: the most relevant result is the coupling of the indentation measurement with 3D imaging, to be able to observe (and quantify) in a 4D fashion the deformation of the sample while applying the load on the indenter tip.

3.2 Analysis of the deformation via Digital Volume Correlation

With the increase of the X-ray imaging instrumentation capabilities to provide 4D datasets, techniques aiming at quantifying local displacements such as DVC become more and more utilized (starting from Bay et al., 1990; to other works including in situ mechanical tests such e.g. Forsberg et al., 2011; Rethore et al., 2011) and this includes also one case of indentation in a foamed plaster sample (Bouterf et al., 2014). Conventional indentation tests are typically 2.5D measurements, and the local deformation in the sample is not a directly-accessible information. Post-experiment measurements on the indented volume can provide some limited 3D information, but the collected data only represent the final stage of the process and the -fundamental- dynamic part of the indentation process is lost (though interesting nano-indentation experiments followed by focused ion beam scanning electron microscopy techniques, including electron back-scattering diffraction to obtain crystallographic information, are employed in metals to obtain important information about crystallography and grain boundaries changes, e.g. Demir et al., 2009; Rueda et al., 2013). In the present work we run a DVC analysis of the local deformation along the whole indentation curve. The microstructure of the shale sample is excellent in providing tracking features for the correlation process, not requiring the utilization of fiducials artificially introduced in the sample, nor specific data pre-processing. The volume renderings of the sample at the beginning and at the end of the loading stage are presented in Fig. 2, while the full sequence is presented as a movie in the Supplementary Material SM2. From the sequence, some important qualitative information can be obtained: the sample behaves in a mixed ductile/brittle behavior. There is plastic deformation, where the shale deforms in the vicinity of the indenter tip, but there's also a markedly brittle behavior highlighted by the development of cracks. The visible anisotropy of this material does have a role in the material behavior, as well as the specific micro-fabric (layers with different mechanical properties) of the shale. It is clear that the crack develops sub-parallel to the bedding, starting close to the indenter imprint. In addition to that, the crack develops in a lamina of a slightly lighter color (more X-ray attenuating layer). The mineralogical composition of the sample suggests a larger amount of carbonates in the layer. Being the X-ray attenuation not concentrated in specific grains (e.g. bioclasts), it is safe to assume that the layer is richer in dolomite acting as a cementing phase, thus making that lamina more brittle than the surrounding material richer in clays, lithics, and organics. DVC has been applied to this series of data to obtain a better view of the deformation mechanism, and a better quantification of it. The DVC analysis provides three volumes with the local (node-specific) displacements along the Cartesian directions, a volume for each loading interval. To better display and analyze the process as a whole, we additionally did two operations: i) we measured the cumulative strain, by progressively adding the sum of the previous deformation fields to each dataset. ii) The geometry of the experiment is axial, therefore the displacements in X and Y can be reduced to a cylindrical symmetry, by providing the radial strain using the center of the indenter tip as the axis of the system. The cumulative deformation of the axial and radial strains of the first and last steps in loading curve is provided in Fig. 3 (the movie with the full sequence is available in the Supplementary Material SM3). The step-by-step strain distribution in the three orthogonal directions has been plotted in Fig. 4. In this case the strain has been calculated by subtracting to the local displacement values the rigid translation component in the respective directions. While for the X and Y directions the radial strain is much more effective for data visualization, the separation of the X and Y components is more efficient in highlighting the anisotropic behavior of the sample, also considering that the sample has been oriented with the lamination parallel to X. Summarizing, for displaying properties the cumulative displacement values, and a single radial value for the XY plane is more informative and allows a better global grasp on the progressive evolution of the system. On the other hand, for the quantitative analysis, a step-by-step analysis and the separated analysis along X, Y, and Z can provide more precise references about the dynamics of process. In Fig. 3 it is possible to observe the cumulative displacements along Z, on the left column: the material pushed down by the indenter tip during the load is evident. At first sight it appears like a plastic deformation, but when looking more closely at the left side of the high displacement zone, a plane in the deformation field becomes evident. This plane is in correspondence with the layer enriched in dolomite previously mentioned. While no evident fracture is visible just under the indenter tip, a high shear layer (not clearly visible from the volume renderings) is highlighted by the DVC. The presence of this shear layer is also visible from the radial displacement field (right column), in the part of the sample with the highest deformation. The presence of this more rigid layer in between two more organics-rich ductile layers allowed the sample to deform more than the opposite side, with the shear plane being generated at the boundary and pushed along the stress direction, but also radially, showing a more brittle fashion than the opposite side of the sample. To better understand the deformation mechanism of the sample, the local strain frequency histograms plotted in Fig. 4 can give more information: concerning the vertical displacements, the sample is progressively pushed downwards and the curves highlight the evolution from a simple displacement as a whole (especially evident in the offset with the sharp and slightly asymmetric peak shape of the first loading step) towards a volume where the displacements have a different structure (enlargement of the peak, growth of secondary peaks/shoulders), highlighting the increasing complexity of the deformation mechanism. The strain in X and Y directions also highlights an increasing complexity: the starting peak evolves by splitting into two peaks while the indenter probe enters the sample. But the behavior for X (parallel to bedding) and Y (perpendicular to bedding) is different. The strain along X is very regular: the peak of the strain distribution becomes wider and eventually splits into two peaks symmetrically, when the indenter pushes sideways the shale along the bedding. On the other hand, in the Y direction the strain starts as a single (sharper) peak and the split into two parts is clearly asymmetric. This asymmetry is due to the triggering of the shear plane previously discussed: this shear plane is sub-parallel to the bedding direction, and has both a Z and a radial component, with the radial component being perpendicular to the bedding, therefore it does not impact the behavior observed along X, but it is clearly visible in the Y strain field, highlighted by the presence of the higher peak on the left side of the plot. Overall, the only factor due to the simple presence of layering by itself seems to be the sharpness of the peak at the early deformation stages (a wider -symmetric- peak means more deformation), while the role of the fabric composition clearly has a role in the micro-mechanical response of the sample. It is also worthwhile to remind that the splitting of the peak into two broad peaks also highlights a deformation with a significantly ductile component, since a perfectly brittle material would display two extremely sharp peaks instead (fracturing with rigid displacement of blocks). This analysis highlights the complexity of the system, where not only anisotropy of the material needs to be taken into account (for shales it is often quantified via diffraction techniques, e.g. Wenk et al., 2008), but a precise knowledge of the mineralogical composition *and* microstructure of the component layers have a relevant impact on the general behavior of the sample.

From DVC data, the maximum shear strain field can be calculated, and this is especially interesting for the visualization of fractures and shear bands. In Fig. 5 the maximum shear volume calculated at the last loading stage is plotted: the section is analogue with the one of the volume renderings in Fig. 3, the presence of the sharp shear band previously discussed is the most evident feature, as expected. A high shear zone is also present close to the indenter surface, where the material shears on the sphere surface. Under the indenter tip, a zone with high shear is present along with other planes (on the left side of the sample) compatible with the displacements observed in the strain maps, with the dolomite-rich layer pushed outwards along with the surrounding material, while shearing at the interface with the organics-rich layer. Another significant feature that has not been discussed is also present as a faint (because of its limited amount of shear, being mostly a crack) maximum shear plane: the presence of cracks radiating from the indenter sphere on the sample surface, sub-parallel to the bedding, as first introduced in Fig. 2., and it will be discussed in the next section.

The analysis of the local deformation in the sample during indentation provides unique information about the micro-mechanical response of shale during indentation. The results clearly show how complex this system is. The mechanical behavior of shales, with its classification in "ductile" and "brittle" is often approximated by using their clay content (e.g. Bourg 2015), but -while it could be a valid starting point in an ideal shale- such an approximation cannot be used to infer mechanical properties in shales for unconventional reservoirs. The most evident proof is exactly the shale we analyzed in the present work: given the amount of carbonates, it should display a more markedly brittle behavior, but it does not. Shale microstructure (especially the presence of cementing phases, usually microcrystalline carbonates, vs. the presence of phases as grains dispersed in a matrix, or forming a loose skeleton) and the presence of organic matter can deeply modify the expected mineralogy-based behavior. Moreover, the presence of large amounts of organics, makes also the mechanical properties of the shale more dependent on temperature and pressure (Voltolini et al., 2019; Voltolini, 2020). An additional problem is intrinsic of the specific application of proppant in a fracture: the size of the contacts. The microfabric of the shale plays an important role: if brittle and ductile layers are smaller in size with respect to the grain contact, mixed behaviors such as the one observed in the present indentation measurements are likely to occur, with a mixed brittle/ductile behavior, the development of shear bands and cracks in specific parts of the sample. Where the fabric displays laminations much larger than the proppant-shale contacts the prediction of the general behavior would become more complex, with different behaviors in different parts of the fracture (as directly observed in Voltolini and Ajo-Franklin, 2020, figure 3).

The results from the DVC analysis also highlights a behavior very different from the one observed in other (usually high-) porous media, where the compaction zone under the indenter was the leading process (Suarez-Rivera et al., 1990; Leite and Ferland, 2001; Kadar et al., 2004; Bouterf et al., 2014): while Green River shale is a porous material, the behavior observed is different from the other porous materials, due to its very different composition and microstructure. The volumetric strain calculated under the indenter tip (not shown) is relatively small and highlights that the compaction of the sample, albeit present, is not the main controlling factor in the response of the shale to the indentation.

Indentation + 3D imaging experiments can also be used to estimate the response of the fracture surface to the overburden pressure. In indentation experiments we have available the information of the load on the indenter tip, coupled with the mechanical response of the shale. By choosing specific densities of distribution of proppant on a fracture surface, the distribution of the force on the single grains, and the expected indentation depth and mechanical response, could be estimated. The plots in Fig. 1 clearly show the relationship of the pressure on the spherical indentation and the indentation depth, where a steep increase is present in the first loading stage only (where the contact area is the smallest).

3.3 Analysis of the fractures

The mechanisms of the development of cracks is very important in assessing the micro-mechanical response of a rock, and it is especially important when considering shale source rocks. As anticipated, the cracks evolve in a layer rendered more brittle by the presence of a higher extent of dolomite cementation. To characterize the evolution of this crack, we have mapped the aperture of the crack during the whole experiment. The main crack aperture maps have been generated taking advantage of the planar geometry, by cropping the area with the main crack and applying automated segmentation (Otsu, 1979), to obtain a binary image of the crack. Last, a projection along the perpendicular direction to the crack plane, operated by summing values of the voxels, provided a 2D aperture map of the main crack. The top section of Fig. 6 shows the projection of the main crack, with a color scale proportional to the aperture, for the full loading/unloading cycle. The evolution of the cracks is similar to the one observed in the preliminary tests with other shales (including the more brittle ones) while developing this experimental approach: under the indenter tip, in the region with the most deformed material and the highest compression zone, there is no open crack, but the crack develops as "wings" along the bedding of the shale, starting from the side of the indenter imprint, where a more relatively tensile field exists. It is interesting to observe that during the loading stage the cracks are barely in contact with the indenter probe. A more quantitative analysis, as plotted in the lower section of Fig. 6, shows how the crack develops by displaying an aperture frequency plot. Following the increase of aperture in the different bins we can observe how the smallest aperture (<32 μm) segment increases, then there is a slow progressive decrease before reaching the maximum load stress. This behavior is different for the aperture segment of the crack >45 μm, where the surface amount always increases (including during the unloading section). In Fig. 6 (bottom-right) the evolution of two size segments of fracture are explicitly plotted in function of the position in the compliance curve: it is evident that the thin portion (aperture <32 μm) of the fracture reaches a maximum before the maximum loading stress, and then it slowly starts to decrease, while the largest portion of the crack increases significantly until the maximum load is reached, and during the unloading it keeps slowly increasing. This behavior slightly changes progressively in function of the aperture values, but the plot with only two segments (i.e. "thin" and "wide" portions of the fracture) helps to better clarify the general concept, which is not very clear from the aperture frequency plot. These plots well describe the full dynamics of the crack development: at the early stage the fracture opens regularly, by increasing the thin aperture first, and progressively the larger aperture section, behaving predominantly as a brittle material. Once the indenter tip moves into the shale sample, the large aperture values continue to increase, but the thin aperture amount in the crack decreases. At the later stage, mostly during the unloading stage, the sections with the larger aperture further increase or -later- becomes constant, but the smaller aperture section of the fracture keeps decreasing. This seems to highlight the mixed ductile/brittle behavior, where during the first part of the loading stage a regular progressive increase in aperture values is observed, as it would be in a brittle material. In the next loading stage, the large aperture sections seems to be more dominant in opening, and it keeps increasing, while the small aperture section tends to close, likely by creep. This behavior becomes more evident in the unloading stage, where the crack further increases in aperture for large values, while the small aperture sections keep closing, highlighting a ductile component in the mechanical response. The evolution of this crack once again highlights the complexity of the micro-mechanics of this sample, with a mixed brittle/ductile behavior present in the most brittle part of the sample as well, where a tensile crack developed, but a ductile component makes it evolve in a rather complex fashion, with a sort of self-sealing component observed in the thinnest portion of the crack only.

3.4 Modeling of the experiment

The modeling was performed first to try to match the loading-unloading indentation curve shown in Fig. 1a and then to reproduce and explain the observed mixed ductile-brittle mechanical behavior, including ductile compaction and brittle fracturing. In the modeling, we assumed perfectly vertical bedding, while in the experiment the bedding orientation slightly deviates from vertical. Assuming uniform and vertical bedding enable us to construction of a quarter symmetric model with two vertical symmetry planes crossing the indentation mark. The quarter symmetric model is computationally efficient and facilitate visualization on vertical cut surfaces that are oriented parallel and perpendicular beddings. After a large number of exploratory model simulations we found that it is indeed possible to match the loading-unloading curves in Fig. 1 and to reproduce a mixed ductile-brittle behavior, including the formation of wing cracks propagating from the indenter.

Figure 7 shows the numerical model with the results of different modes of failure at the maximum indentation depth of 0.75 mm. The figure shows a large zone of plastic yielding in shear beneath the indenter in, whereas a wing shaped crack has formed on the side of the indenter. The model is discretized into cubical elements with 0.1 mm side length with the discrete fracture formed by tensile failure of elements along the direction of the weak planes. The shape of the indentation and the wing shaped cracks are in good agreement with that observed from the X-ray micro-images in Fig. 3 and 6. The key for obtaining such a good visual match with experimental observations is to consider the anisotropic material behavior of the shale, including matrix shear strength parameters (cohesion and friction angle) and tensile strength of weak planes along the bedding. The material parameters for the results in Fig. 7 are listed in Table 2. In addition, the model includes one column of elastic boundary elements at the lateral surface of the shale sample to simulate the deformation effects of the 1 mm thick aluminum sleeve and the epoxy-filled gap between the sample and the sleeve. The impact of the different parameters on the modeling results is discussed in the next sections related the analysis of load-indentation curve, fracturing, and sample deformation.

3.4.1. Analysis of the load-indentation curve

The shape of the load-indentation curve depends on the elastic and shear strength properties of the rock matrix in the anisotropic ubiquitous joint model. We also found that the friction at the interface between the Brinell indenter and the shale surface has a significant impact on the results. Fig. 8 presents model simulation results with a good match to the experimental results for the case of an indenter-shale interface friction angle of ϕ_{is} = 20°. The elastic properties, i.e. Young's modulus and Poisson's ratio impact both the loading and unloading curves, but can be calibrated against observed displacement rebound during unloading. As in the analytical analysis of the unloading curve we found that the value of E = 5.95 MPa and a Poisson's ration of 0.35 provides a good match between simulation and experiment for the unloading curve (Fig. 8). The indentation during loading is dominated by the shear plastic yielding and depends strongly on the shear strength properties of the matrix, i.e. matrix cohesion (C_m) and friction angle (ϕ_m). There is some non-uniqueness in choosing the values of the matrix cohesion (C_m) and friction angle (ϕ_m) as a good match to the loading curve can be achieved using different combinations of cohesion and friction angle. The results shown in Fig. 8 is for C_m = 5 MPa, ϕ_m = 27°, but identical results was obtained for the combination C_m = 10 MPa, ϕ_m = 18°. Another parameter that impacts the load-indentation curve is the friction properties of the interface between the indenter probe and the shale surface. To illustrate the impact of the indenter-shale interface friction, Figure 8 also shows an alternative simulation results for an almost frictionless indenter-shale interface (ϕ_{is} = 4°). With this frictionless interface, a bulged curve is achieved that does not follow the straighter experimental curve and the simulated peak load becomes much smaller. The peak load could have been matched also for an indenter-shale interface (ϕ_{is} = 4°) by increasing the shear strength of the sample, but the loading curve would still be too bulged and not match the straighter experimental curve.

Other parameters such as the properties of the weak planes in the model, if varied within reasonable ranges does not have a significant impact on the loading-unloading curves. Moreover, the properties of the outer boundary elements representing the aluminum sleeve and epoxy-filled gap have no significant impact loading-unloading curve. Thus, the loading-unloading indentation curves are dominated by the local elasto-plastic behavior of the matrix rock just below the indenter.

3.4.2 Analysis of displacement and strain fields

An analysis of the displacement and strain fields provides some additional information that can be used to constrain material parameters. One distinct feature in this context is the pattern of a heave or pileup that can occur on the side of the indenter. Fig. 9 shows the vertical displacement and deformed mesh for the two different cases of indenter-shale interface friction. When looking at the experimental images in Fig. 3, it appears that the pileup on the side of the indenter is non-existent. The modeling show that some frictional resistance of the indenter-shale contact is necessary to avoid a pileup. Moreover, in the case of higher friction at the indenter-shale contact (ϕ_{is} = 20°), the vertical displacement field propagates much further down below the indenter. This is more similar to the vertical displacement pattern observed in the experiments as shown in Fig. 3.

Sensitivity studies showed that the pileup is also impacted by the combination of C_m and ϕ_m of the shale matrix and by the shear properties of the weak planes (C_{wp} and ϕ_{wp}) in the ubiquitous joint model. The combination of low-C_m-high-ϕ_m for the matrix, results in a larger pileup than for the combination of high-C_m-low-ϕ_m. In one case, we simulated a much lower friction angle and hence a lower frictional strength along vertical weak planes (ϕ_{wp} = 20° for vertical weak planes compared to ϕ_m = 27° in the matrix). Such reduction in the weak-plane shear strength caused anisotropy in the pileup and vertical displacement that cannot be observed in the experiments.

Another evidence of the impact of the indenter-shale interface friction is the maximum shear strain. Fig. 10 shows that in the case of a low friction indenter-shale interface (ϕ_{is} = 4°), the maximum shear strain is localized close to the indenter. This localized shear strain involves compaction normal to the indenter surface while expansion tangential to the indenter surface. In the case of a higher indenter-shale interface friction (ϕ_{is} = 20°), such expansion in the tangential direction is restricted. Instead, shear bands forms and shear deformations occur farther below the indenter. This pattern seems more consistent with that of the experiment shown in Fig. 5. However, a more heterogeneous shear pattern is observed in Fig. 5, due to micro-heterogeneities in shale properties that are not considered in the current model.

3.4.3 Analysis of fracture

The fracturing occurring from the indenter and propagation outwards towards the boundary of the sample was successfully modeled as shown in Fig. 7. Moreover, as in the experiment, the modeling could reproduce the fact that no fracture could be observed beneath the indenter. Beneath the indenter the mechanical responses is dominated by a ductile shear yielding response in the rock matrix. In the model, the fracture initiated and propagated along the bedding and started from the indenter as observed in the experiment. The fracture initiation is determined by the tensile strength of the weak planes, which in the model was set lower that the tensile strength of the matrix (Table 2). The numerical modeling showed that the micromechanical response involves a competition between ductile shear yielding and brittle fracturing. Below the indenter, plastic yielding occurs first and prevent tensile fracturing in that area. The fracture can propagation outwards from the indenter if considering a brittle tensile failure by dropping the tensile strength to zero after a small tensile plastic strain. Without applying such a strain softening, the modeling shows that the fracture could not propagate away from the indenter. The lateral boundary condition of the model also affects the fracture propagation. The 1-mm thick aluminum sleeve and the epoxy-filled gap provide some lateral deformability that was simulated by one column of elastic elements with a Young's modulus of 0.8 GPa. If assuming a completely rigid boundary on the sample, the simulations showed that the fracture cannot propagate far from the indenter. Fig. 11 shows the calculated fracture aperture based on the plastic tensile strain normal to the weak planes and element thickness. The aperture is up to 30 microns, which appears to be equivalent to the most frequent aperture of the experiment estimated from the X-ray imaging in Fig. 6.

4. Conclusions

Indentation tests are a quick and well-established measurement used to better understand the micro- and nano- mechanical properties of materials. Indentation methods are rather routinely used for characterization of shales as well. Given the nature of the material, nano-indentation has been used to better understand the mechanical properties of single components (e.g. kerogen particles), or the very localized mechanical response of a composite matrix made of a small number of components (Kumar et al., 2012; Shukla et al., 2013; Bennett et al., 2015; Liu et al., 2016; Veytskin et al., 2017), to better understand the upscaling properties of shales. To obtain more generalized properties, micro-indentation has been widely used as well (Ulm and Abousleiman, 2006; Han et al., 2015; Ping et al., 2015), including to estimate properties such as fracture toughness and fracability (Mullen and Enderlin, 2012; Zeng et al., 2019). The micro-mechanical properties of shales become especially important when considering unconventional oil and gas recovery, where the usable lifetime of fractures is deeply linked to the micro-mechanical properties of the proppant-shale contacts. In this work we have proposed a novel approach for micro-mechanical testing on shales that overcomes most of the limitations encountered with conventional indentation tests. While this approach is still in its infancy, as well as extremely complicated and time-consuming, it has proven effective in providing an unprecedented amount of information, and revealed its potential for future improvements in dedicated instrumental setups and to operate at extreme conditions as well.

The micro-mechanical modeling of the indentation tests and X-ray micro images provides an unique opportunity to characterize the mechanical properties relevant for predicting proppant and fracture closure evolution during production from unconventional hydrocarbon reservoirs. The combination of matching the loading-unloading indentation curve and high resolution displacement field images in three dimensions can provide for a way of constraining elasto-plastic material parameters and strength anisotropy. This includes any anisotropy in the displacement field or the degree of pileup adjacent to the indenter. The modeling confirmed observations and interpretations made from the experiments. The loading-unloading indentation curve shows significant irreversible indentation in a mixed ductile (prevalent) - brittle mechanical response that was determined by the matrix elasto-plastic properties of the shale, whereas the properties of weak planes did not have a significant impact on the indentation depth. Moreover, the modeling confirmed that the formation of the brittle fracture had no significant impact on the load-indentation curve. The fictional strength properties of the indenter-shale interface is a parameter that has a significant impact on the micromechanical behavior and this parameter should be characterized as accurately as possible. The current modeling was conducted for homogenous shale properties, while micro-heterogeneities such as more brittle and rigid layers would be required to model some of the heterogeneous observed in the X-ray micro images.

This opens many opportunities for the unconventional reservoirs exploitation studies (e.g. studying the micro-mechanical response in detail at realistic P/T/chemistry reservoir conditions), but also for Materials Sciences in general. While simple indentation + imaging tests have been performed in building materials at ambient conditions, we can expect this approach to draw attention to solve problems concerning the micro-mechanical behavior of a large class of materials at non-ambient conditions, e.g. to understand how the mechanical response of a material changes with temperature. This specific question is also valid for the oil and gas shale community, where shales with large amounts of organic material are expected to display a transition from mostly brittle to mostly ductile, thus having a huge impact in the prediction of the usable life of wells, and the mechanical evolution of fractures in general during and after the fracturing process. A comprehensive knowledge of the micro- and larger scale mechanical response of fractures in shales would also help in evaluating new hydraulic fracturing procedures and additional treatments targeting the controlled modification of the surfaces of the fractures mechanical properties (e.g. making them mechanically stronger, more porous, etc.), thus helping in mitigating the use of water in fracking and re-fracking events, and helping in understanding the problem of induced seismicity.

Acknowledgements

MV carried out the work under the award FWP FP00008049 "A New Framework for Microscopic to Reservoir-Scale Simulation of Hydraulic Fracturing and Production: Testing with Comprehensive Data from HFTS and Other Hydraulic Fracturing Field Test Sites" and NETL ESD14089 award at the LBNL: "Numerical and Laboratory Investigations for Maximization of Production from Tight/Shale Oil Reservoirs: From Fundamental Studies to Technology Development and Evaluation". The numerical modeling work was conducted under the project *Field Evaluation of the Caney Shale as an Emerging Unconventional Play, Southern Oklahoma* with financial support by the U.S. Department of Energy, Office of Fossil Energy, Office of Natural Gas and Petroleum Technology, through the National Energy Technology Laboratory and Oklahoma State University, under Award Number DE-AC02-05CH11231. This research used resources of the Advanced Light Source, which is a DOE Office of Science User Facility under contract no. DE-AC02-05CH11231, and Dula Parkinson and the staff at beamline 8.3.2. are acknowledged for their help during data acquisition. Alan Burnham and Total are acknowledged for providing the Green River shale sample.

Table 1

Mineral species	*Weight [%]*
Quartz	20.5(5)
Albite	13.5(4)
Pyrite	0.4(1)
Analcime	7.9(2)
Calcite	1.2(1)
Dolomite	46.0(8)
Illite	9.2(6)
I/S	1.3(9)

Rietveld analysis of the Green River Shale sample XRD profile. The illite-smectite (I/S) phase has been used to take into account the asymmetry of the illite peak. Results are given in weight percentages, and the estimated error of the last digit from the fit is given in parenthesis. Minerals have been divided into three groups (top to bottom): lithics, carbonates, and clays.

Table 2. Material properties used for the numerical modeling of the indentation on Green River Shale sample

Parameter	Value
Young's modulus, E [GPa]	5.95
Poisson's ratio, ν [-]	0.35
Matrix cohesion, C_m [MPa]	5
Matrix friction angle, ϕ_m [°]	27°

Matrix tensile strength, T_m [MPa]	10
Weak-plane cohesion, C_{wp} [MPa]	5
Weak-plane friction angle, ϕ_{wp} [°]	27°
Weak-plane tensile strength, T_{wp} [MPa]	5.2 → 0[a]
Intender-shale interface friction angle, ϕ_{is} [°]	20°

[a)]The tensile strength drops to zero after a plastic strain of 0.001 (strain softening)

Figure captions:

Fig. 1

In a) the full compliance curve (loading and unloading) of the indentation experiments has been plotted. For each increase in load, the indentation depth has been calculated from the radiographs. The loading steps where radiographs have been collected are marked with diamonds. In red are marked the steps where a full tomographic dataset was also recorded, for a total of 12 tomographic volumes. In b) the calculated pressure on the indentation imprint is plotted (equivalent to Meyer hardness).

Fig. 2

Series of volume renderings showing the sample at zero loading (top row), and maximum load (bottom). From left to right, the volume renderings display the sample as: viewed from the top, virtually cut normal with respect to the bedding, under the indenter tip, and cut parallel to the bedding.

Fig. 3

Cumulative strain along the Z axis (left column), and the radial (XY plane) strain (right column) of the sample at the first and last steps of the loading curve. The volume rendering of the sample (minus the indenter sphere) has been superimposed to the volumes calculated from the DVC results (in color). Volumes are vertical cuts normal to the bedding, similar to the center column in Fig. 2. The full sequence is presented as a movie in the supplementary material SM3.

Fig. 4

Frequency plots of the strain in the sample along the three Cartesian directions between each step during loading. X and Y are here separated to highlight the anisotropic behavior of the sample due to the bedding, which would have been lost if plotting the radial coordinates, better for plotting figures in axial systems, as in Fig. 3.

Fig. 5

Maximum shear strain volume calculated at the last loading step. The main shear band (see text for comprehensive description) becomes extremely evident in this kind of analysis.

Fig. 6

Crack analysis of the sample. On the top the color-labeled aperture maps of the crack for the full compliance curve are shown. Botton-left, the frequency plots of the fracture aperture values are plotted to evaluate the global evolution of the crack. Bottom-right the plot showing the evolution of the thinner and thicker segments of the fracture have been plotted to better highlight how the behavior of the crack expansion changes in function of the position in the indentation curve.

Fig. 7

Numerical model grid of the quarter symmetric model with results of deformed mesh and distribution of failure modes, including brittle tensile failure along weak planes and shear failure of the matrix at the maximum indentation depth of 0.75 mm and indenter load of 78 kgf.

Fig. 8

Indenter loading-unloading curves from experimental data in Figure 1 with comparison to simulated loading-unloading curves from modeling considering two different values of indenter-shale interface friction (ϕ_{is} = 20 and ϕ_{is} = 4) with other material parameters of the shale listed in Table 2.

Fig. 9

Simulation results of vertical displacement and deformed mesh considering two different values of indenter-shale interface friction (ϕ_{is} = 20 and ϕ_{is} = 4) with other material parameters of the shale listed in Table 2.

Fig. 10

Simulation results of maximum shear strain considering two different values of indenter-shale interface friction (ϕ_{is} = 20 and ϕ_{is} = 4) with other material parameters of the shale listed in Table 2.

Fig. 11. Simulation results of fracture aperture as calculated from plastic normal strain within the tensile fracturing zone.

References

Agapito, J., and Hardy, M., 1982. Induced horizontal stress method of pillar design in oil shale. In *Proc. 15th Oil Shale Symposium, Colorado School of Mines, Golden, 1982* (pp. 191-197).

Bay, B.K., Smith, T.S., Fyhrie, D.P. and Saad, M., 1999. Digital volume correlation: three-dimensional strain mapping using X-ray tomography. *Experimental mechanics*, *39*(3), pp.217-226.

Bennett, K.C., Berla, L.A., Nix, W.D. and Borja, R.I., 2015. Instrumented nanoindentation and 3D mechanistic modeling of a shale at multiple scales. *Acta Geotechnica*, *10*(1), pp.1-14.

Bourg, I.C., 2015. Sealing shales versus brittle shales: a sharp threshold in the material properties and energy technology uses of fine-grained sedimentary rocks. *Environmental Science & Technology Letters*, *2*(10), pp.255-259.

Bouterf, A., Roux, S., Hild, F., Adrien, J., Maire, E. and Meille, S., 2014. Digital Volume Correlation Applied to X-ray Tomography Images from Spherical Indentation Tests on Lightweight Gypsum. *Strain*, *50*(5), pp.444-453.

Chateigner, D., 2013. *Combined analysis*. John Wiley & Sons.

Chengzao, J., Zheng, M. and Zhang, Y., 2012. Unconventional hydrocarbon resources in China and the prospect of exploration and development. *Petroleum Exploration and Development*, *39*(2), pp.139-146.

Demir, E., Raabe, D., Zaafarani, N. and Zaefferer, S., 2009. Investigation of the indentation size effect through the measurement of the geometrically necessary dislocations beneath small indents of different depths using EBSD tomography. *Acta Materialia*, *57*(2), pp.559-569.

Dierick, M., Masschaele, B. and Van Hoorebeke, L., 2004. Octopus, a fast and user-friendly tomographic reconstruction package developed in LabView®. *Measurement Science and Technology*, *15*(7), p.1366.

Eseme, E., Urai, J.L., Krooss, B.M. and Littke, R., 2007. Review of mechanical properties of oil shales: implications for exploitation and basin modelling. *Oil Shale*, *24*(2).

Fischer-Cripps, A.C., 2011. Applications of Nanoindentation. In *Nanoindentation* (pp. 213-233). Springer, New York, NY.

Forsberg, F., Sjödahl, M., Mooser, R., Hack, E. and Wyss, P., 2010. Full Three‐dimensional strain measurements on wood exposed to three‐point bending: analysis by use of digital volume correlation applied to synchrotron radiation micro‐computed tomography image data. *Strain*, *46*(1), pp.47-60.

Han, Q., Chen, P. and Ma, T., 2015. Influencing factor analysis of shale micro-indentation measurement. *Journal of Natural Gas Science and Engineering*, *27*, pp.641-650.

Hart, B., Sayers, C.M. and Jackson, A., 2011. An introduction to this special section: Shales. *The Leading Edge*, *30*(3), pp.272-273.

Itasca, 2011. FLAC3D v5.0, Fast Lagrangian Analysis of Continua in 3 Dimensions, User's Guide, Itasca Consulting Group, Minneapolis, Minnesota.

Joshi, S.D., 1987, January. A review of horizontal well and drainhole technology. In *SPE annual technical conference and exhibition*. Society of Petroleum Engineers.

Kádár, C., Maire, E., Borbély, A., Peix, G., Lendvai, J. and Rajkovits, Z., 2004. X-ray tomography and finite element simulation of the indentation behavior of metal foams. *Materials Science and Engineering: A*, *387*, pp.321-325.

Knaus, E., Killen, J., Biglarbigi, K. and Crawford, P., 2010. An overview of oil shale resources. In *Oil Shale: A Solution to the Liquid Fuel Dilemma* (pp. 3-20). American Chemical Society.

Kumar, V., Curtis, M.E., Gupta, N., Sondergeld, C.H. and Rai, C.S., 2012, January. Estimation of elastic properties of organic matter in Woodford Shale through nanoindentation measurements. In *SPE Canadian Unconventional Resources Conference*. Society of Petroleum Engineers.

Leite, M.H. and Ferland, F., 2001. Determination of unconfined compressive strength and Young's modulus of porous materials by indentation tests. *Engineering geology*, *59*(3-4), pp.267-280.

Li, Q., Jew, A.D., Kohli, A., Maher, K., Brown Jr, G.E. and Bargar, J.R., 2019. Thicknesses of Chemically Altered Zones in Shale Matrices Resulting from Interactions with Hydraulic Fracturing Fluid. *Energy & Fuels*, *33*(8), pp.6878-6889.

Liang, F., Sayed, M., Al-Muntasheri, G.A., Chang, F.F. and Li, L., 2016. A comprehensive review on proppant technologies. *Petroleum*, *2*(1), pp.26-39.

Liu, K., Ostadhassan, M. and Bubach, B., 2016. Applications of nano-indentation methods to estimate nanoscale mechanical properties of shale reservoir rocks. *Journal of Natural Gas Science and Engineering*, *35*, pp.1310-1319.

MacDowell, A.A., Parkinson, D.Y., Haboub, A., Schaible, E., Nasiatka, J.R., Yee, C.A., Jameson, J.R., Ajo-Franklin, J.B., Brodersen, C.R. and McElrone, A.J., 2012, October. X-ray micro-tomography at the Advanced Light Source. In *Developments in X-Ray Tomography VIII* (Vol. 8506, p. 850618). International Society for Optics and Photonics.

Mullen, M.J. and Enderlin, M.B., 2012, January. Fracability index-more than rock properties. In *SPE Annual Technical Conference and Exhibition*. Society of Petroleum Engineers.

Otsu, N., 1979. A threshold selection method from gray-level histograms. *IEEE transactions on systems, man, and cybernetics*, *9*(1), pp.62-66.

Ping, C.H.E.N., Qiang, H.A.N., Tianshou, M.A. and Dong, L.I.N., 2015. The mechanical properties of shale based on micro-indentation test. *Petroleum exploration and development*, *42*(5), pp.723-732.

Réthoré, J., Limodin, N., Buffiere, J.Y., Hild, F., Ludwig, W. and Roux, S., 2011. Digital volume correlation analyses of synchrotron tomographic images. *The Journal of Strain Analysis for Engineering Design*, *46*(7), pp.683-695.

Rueda, A.O., Seuba, J., Anglada, M. and Jiménez-Piqué, E., 2013. Tomography of indentation cracks in feldspathic dental porcelain on zirconia. *Dental Materials*, *29*(3), pp.348-356.

Rutqvist, J., 2017. An overview of TOUGH-based geomechanics models. *Computers & Geosciences*, *108*, pp. 56-63.

Rutqvist, J. and Tsang, C.-F., 2002. A study of caprock hydromechanical changes associated with CO2 injection into a brine aquifer. *Environmental Geology*, *42*, 296-305.

Rutqvist, J., Zheng, L., Chen, F, Liu, H.-H. and Birkholzer, J., 2014. Modeling of Coupled Thermo-Hydro-Mechanical Processes with Links to Geochemistry Associated with Bentonite-Backfilled Repository Tunnels in Clay Formations. *Rock Mechanics and Rock Engineering*, 47, 167–186.

Rutqvist, J., Rinaldi, A.P., Cappa, F., and Moridis, G.J., 2015. Modeling of fault activation and seismicity by injection directly into a fault zone associated with hydraulic fracturing of shale-gas reservoirs. *Journal of Petroleum Science and Engineering*, *127*, pp. 377–386.

Saif, T., Lin, Q., Butcher, A.R., Bijeljic, B. and Blunt, M.J., 2017. Multi-scale multi-dimensional microstructure imaging of oil shale pyrolysis using X-ray micro-tomography, automated ultra-high resolution SEM, MAPS Mineralogy and FIB-SEM. *Applied energy*, *202*, pp.628-647.

Schindelin, J., Arganda-Carreras, I., Frise, E., Kaynig, V., Longair, M., Pietzsch, T., Preibisch, S., Rueden, C., Saalfeld, S., Schmid, B. and Tinevez, J.Y., 2012. Fiji: an open-source platform for biological-image analysis. *Nature methods*, *9*(7), pp.676-682.

Shukla, P., Kumar, V., Curtis, M., Sondergeld, C.H. and Rai, C.S., 2013, January. Nanoindentation studies on shales. In *47th US Rock Mechanics/Geomechanics Symposium*. American Rock Mechanics Association.

Suarez-Rivera, F.R., Cook, N.G.W., Cooper, G.A. and Zheng, Z., 1990, January. Indentation by pore collapse in porous rocks. In *The 31th US Symposium on Rock Mechanics (USRMS)*. American Rock Mechanics Association.

Tiwari, P., Deo, M., Lin, C.L. and Miller, J.D., 2013. Characterization of oil shale pore structure before and after pyrolysis by using X-ray micro CT. *Fuel*, *107*, pp.547-554.

Tudisco, E., Andò, E., Cailletaud, R. and Hall, S.A., 2017. TomoWarp2: A local digital volume correlation code. *SoftwareX*, *6*, pp.267-270.

Ulm, F.J. and Abousleiman, Y., 2006. The nanogranular nature of shale. *Acta Geotechnica*, *1*(2), pp.77-88.

Veytskin, Y.B., Tammina, V.K., Bobko, C.P., Hartley, P.G., Clennell, M.B., Dewhurst, D.N. and Dagastine, R.R., 2017. Micromechanical characterization of shales through nanoindentation and energy dispersive x-ray spectrometry. *Geomechanics for Energy and the Environment*, *9*, pp.21-35.

Voltolini, M., Kwon, T.H. and Ajo-Franklin, J., 2017. Visualization and prediction of supercritical CO2 distribution in sandstones during drainage: An in situ synchrotron X-ray micro-computed tomography study. *International Journal of Greenhouse Gas Control*, *66*, pp.230-245.

Voltolini, M., Barnard, H., Creux, P. and Ajo-Franklin, J., 2019. A new mini-triaxial cell for combined high-pressure and high-temperature in situ synchrotron X-ray microtomography experiments up to 400° C and 24 MPa. *Journal of synchrotron radiation*, *26*(1), pp.238-243.

Voltolini, M. and Ajo-Franklin, J., 2020. Evolution of propped fractures in shales: The microscale controlling factors as revealed by in situ X-Ray microtomography. *Journal of Petroleum Science and Engineering*, *188*, p.106861.

Voltolini, M., 2020. In-Situ 4D Visualization And Analysis Of Temperature-Driven Creep In An Oil Shale Propped Fracture. *Journal of Petroleum Science and Engineering,* (accepted for publication).

Walle, L.E., Stroisz, A.M., Brevik, N.Ø., Jensen, S.S. and Holt, R.M., 2017, August. Laboratory measurements of strength parameters for fracturing. In *51st US Rock Mechanics/Geomechanics Symposium*. American Rock Mechanics Association.

Wenk, H.R., Voltolini, M., Kern, H., Popp, T. and Mazurek, M., 2008. Anisotropy in shale from Mont Terri. *The Leading Edge*, *27*(6), pp.742-748.

Yang, Z., Wang, L., Chen, Z., Xiang, D., Hou, D., Ho, C.L. and Zhang, G., 2018. Micromechanical characterization of fluid/shale interactions by means of nanoindentation. *SPE Reservoir Evaluation & Engineering*, *21*(02), pp.405-417.

Zeng, Q., Wu, Y., Liu, Y. and Zhang, G., 2019. Determining the micro-fracture properties of Antrim gas shale by an improved micro-indentation method. *Journal of Natural Gas Science and Engineering*, *62*, pp.224-235.

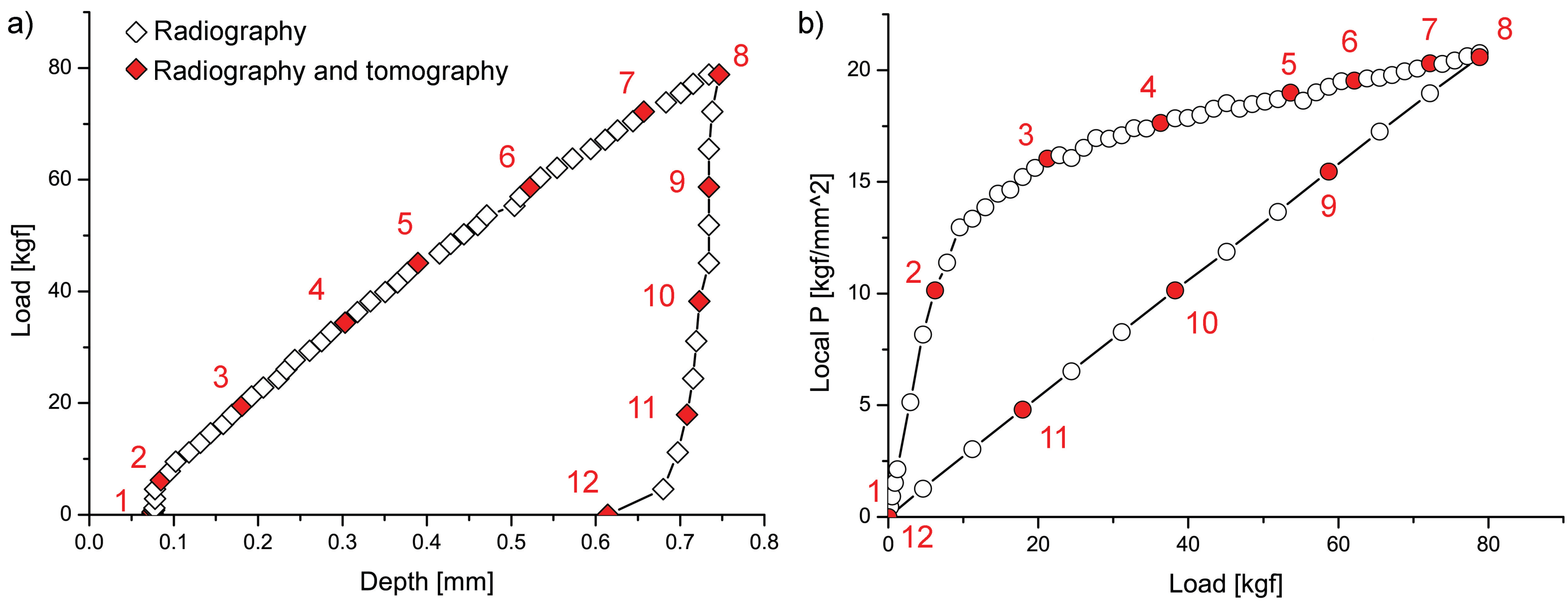

a)
Radiography
Radiography and tomography
Load [kgf]
Depth [mm]
0.0
0.1
0.2
0.3
0.4
0.5
0.6
0.7
0.8
0
20
40
60
80
1
2
3
4
5
6
7
8
9
10
11
12
b)
Local P [kgf/mm^2]
Load [kgf]
0
5
10
15
20
0
20
40
60
80
1
2
3
4
5
6
7
8
9
10
11
12

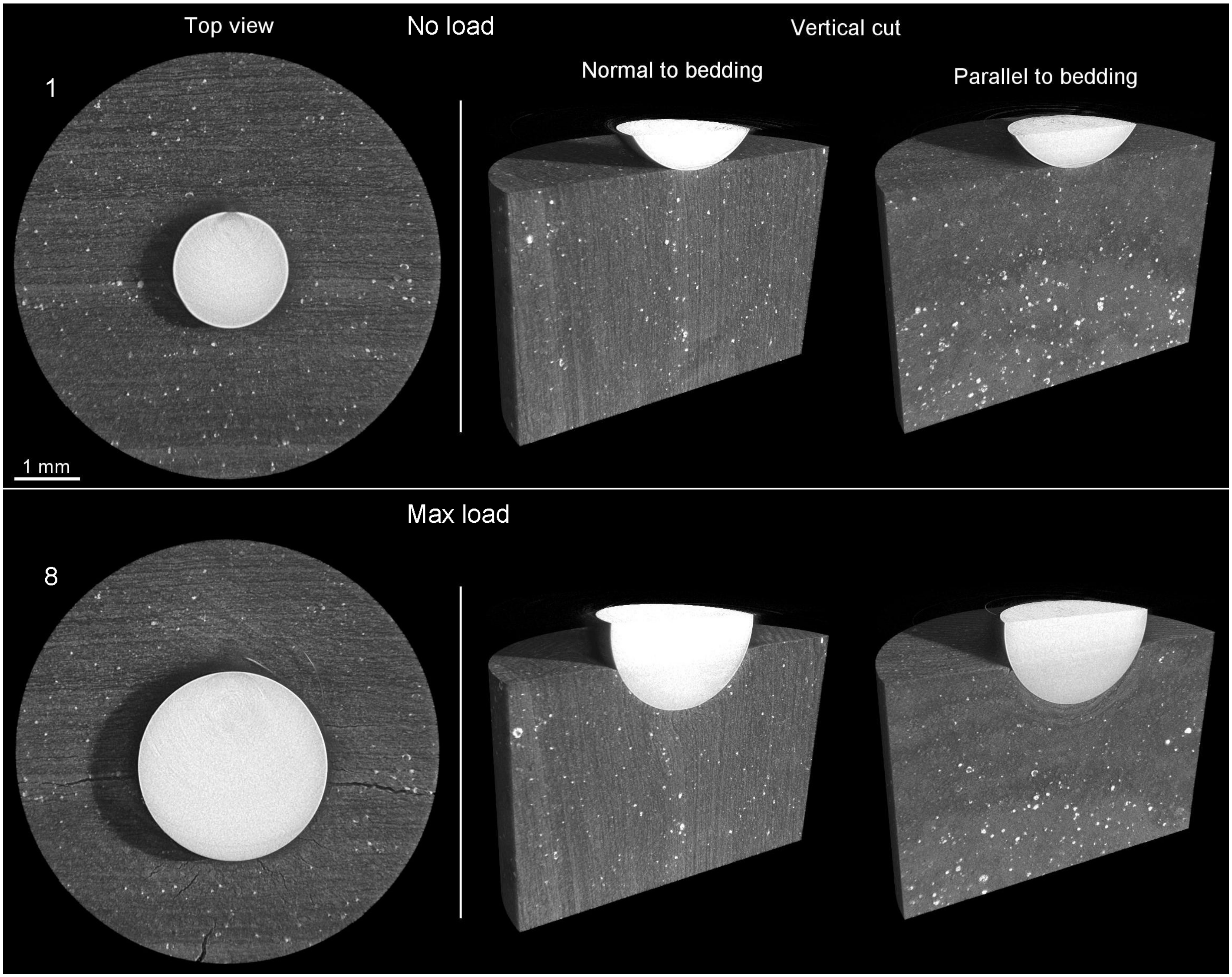

Top view
No load
Vertical cut
Normal to bedding
Parallel to bedding
1
1 mm
Max load
8

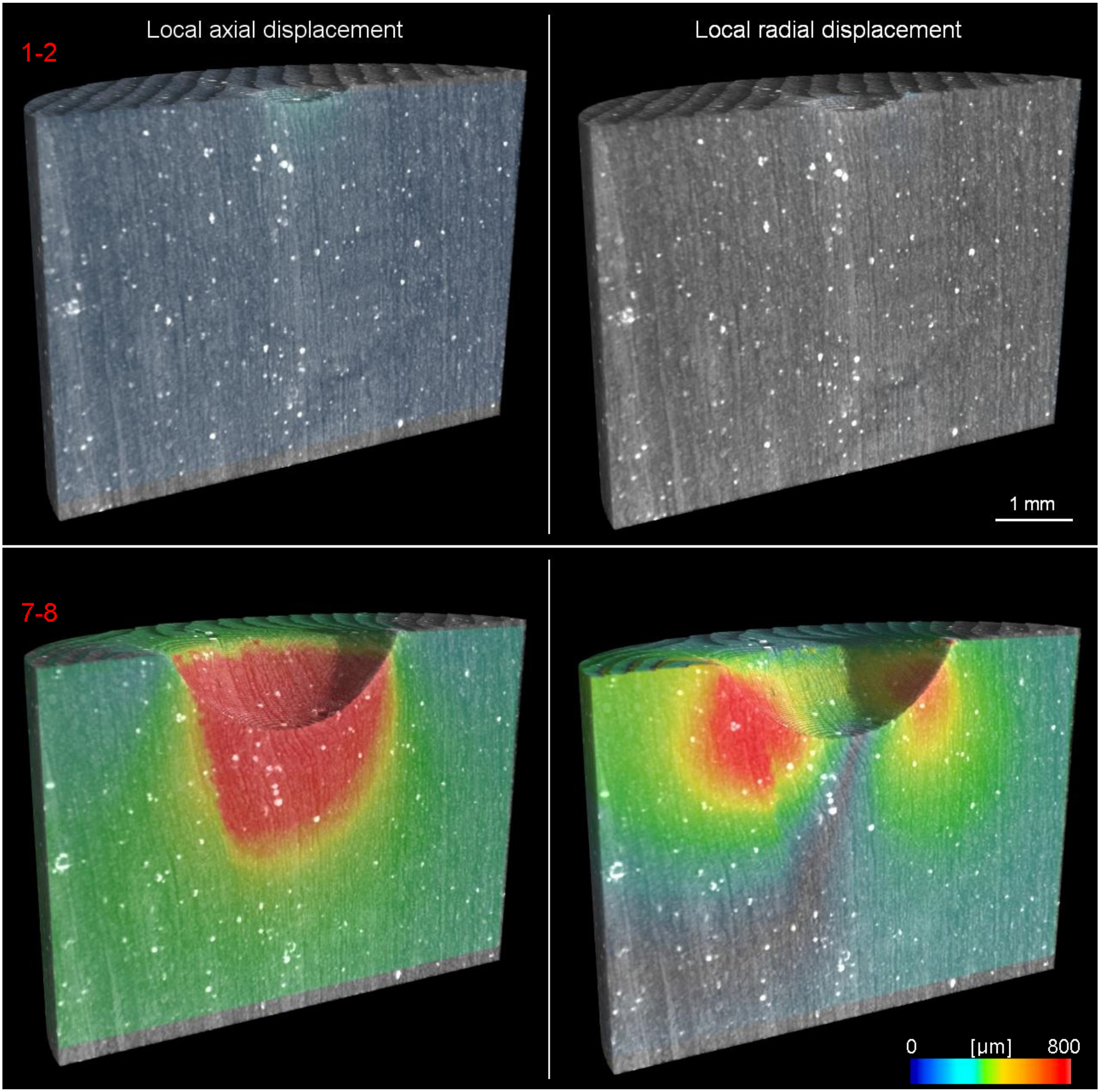

Local axial displacement
Local radial displacement
1-2
1 mm
7-8
0
[µm]
800

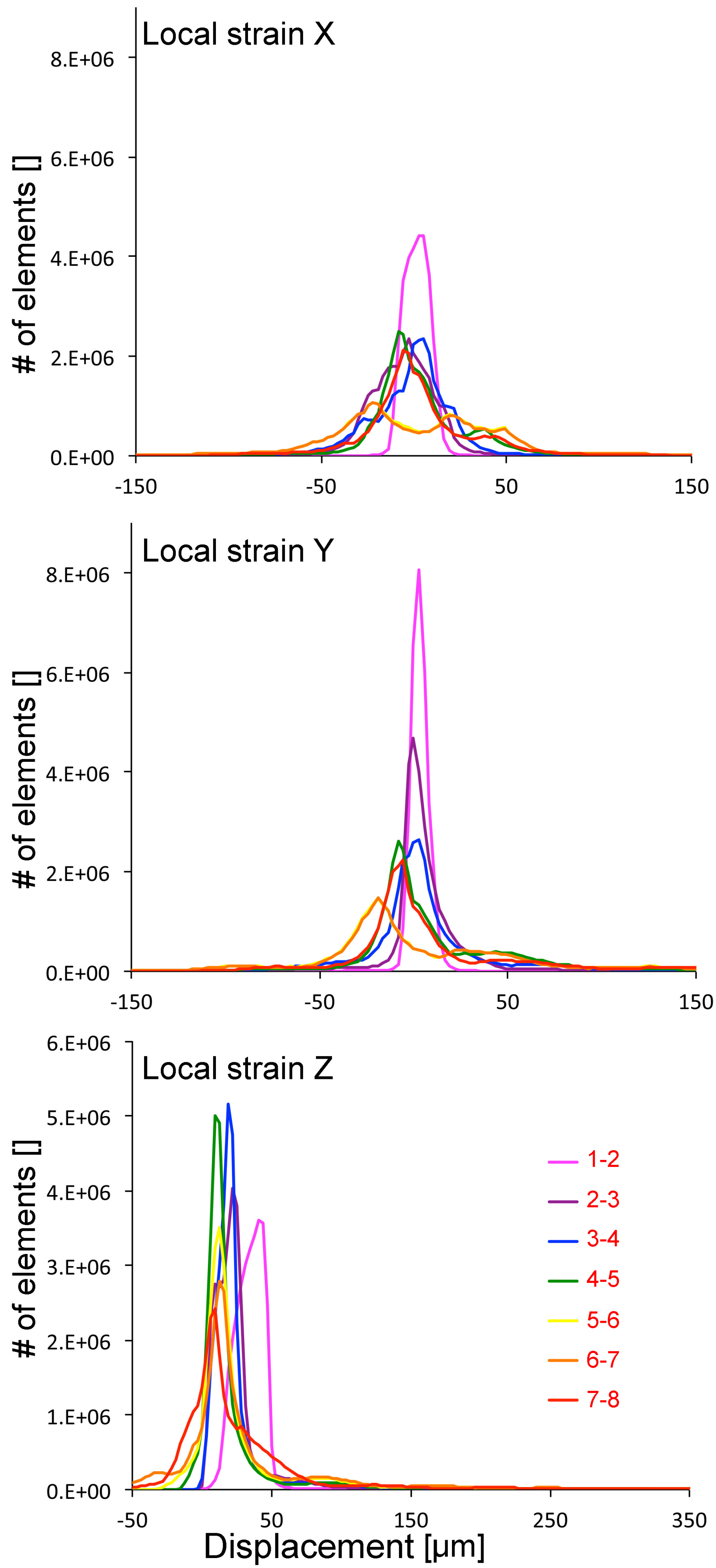
Local strain X
Local strain Y
Local strain Z
# of elements []
8.E+06
6.E+06
4.E+06
2.E+06
0.E+00
5.E+06
3.E+06
1.E+06
-150
-50
50
150
250
350
Displacement [µm]
1-2
2-3
3-4
4-5
5-6
6-7
7-8

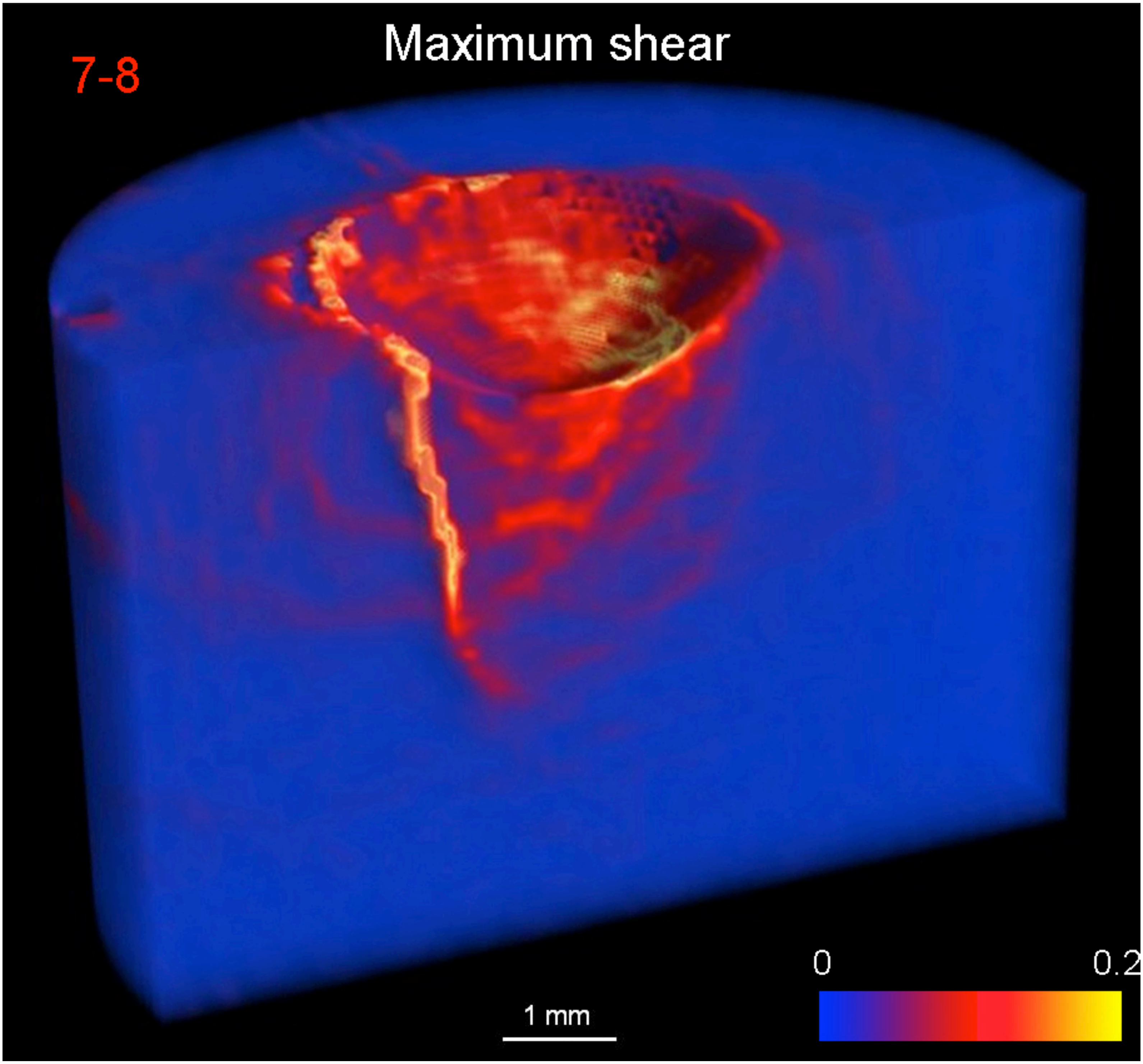
Maximum shear
7-8
0
0.2
1 mm

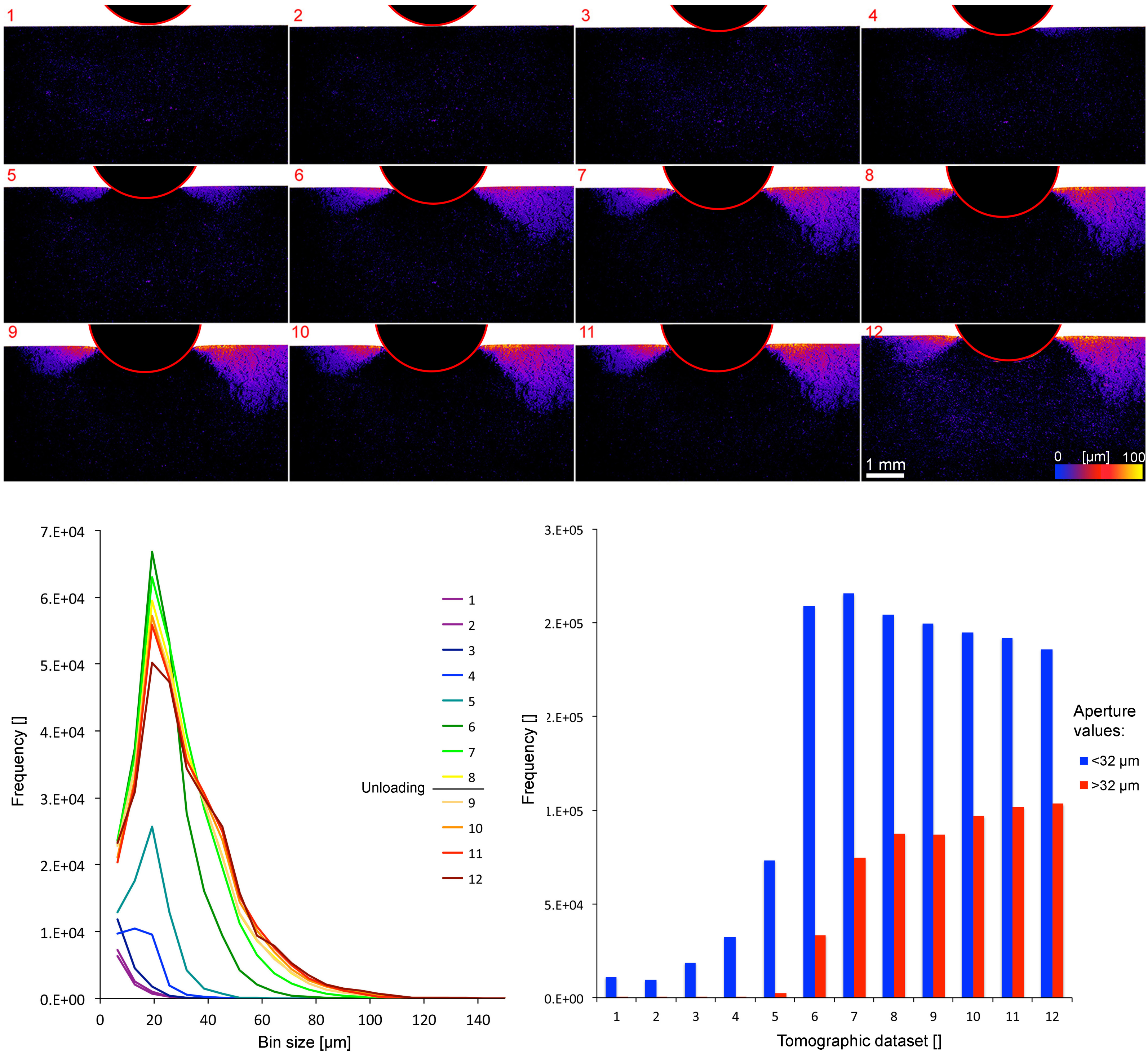

1
2
3
4
5
6
7
8
9
10
11
12
1 mm
0 [μm] 100
7.E+04
6.E+04
5.E+04
4.E+04
3.E+04
2.E+04
1.E+04
0.E+00
Frequency []
0 20 40 60 80 100 120 140
Bin size [μm]
1
2
3
4
5
6
7
8
Unloading
9
10
11
12
3.E+05
2.E+05
2.E+05
1.E+05
5.E+04
0.E+00
Frequency []
1 2 3 4 5 6 7 8 9 10 11 12
Tomographic dataset []
Aperture values:
<32 μm
>32 μm

Quarter Symmetric Model
0.75 mm Indentation at 78 kgf load

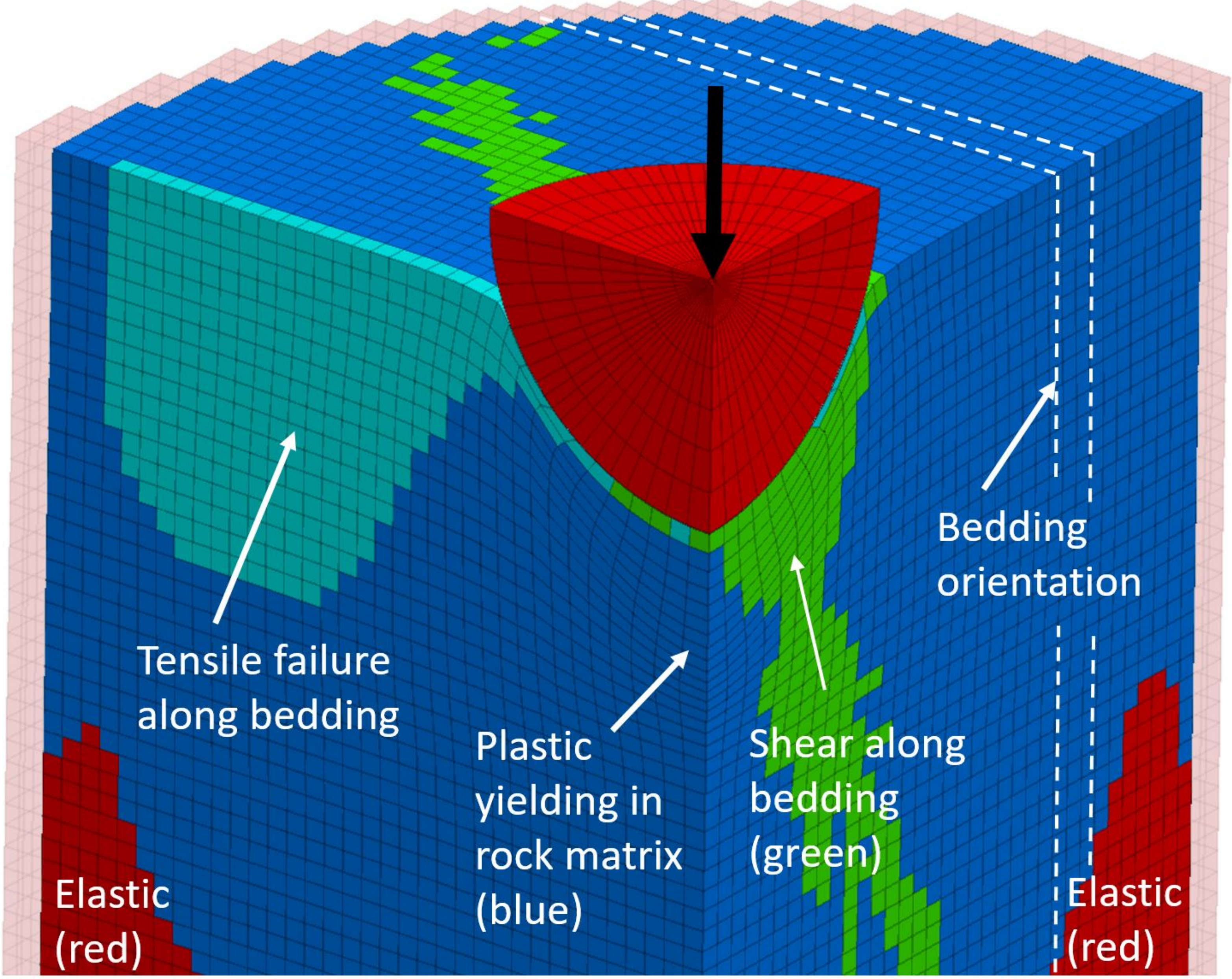

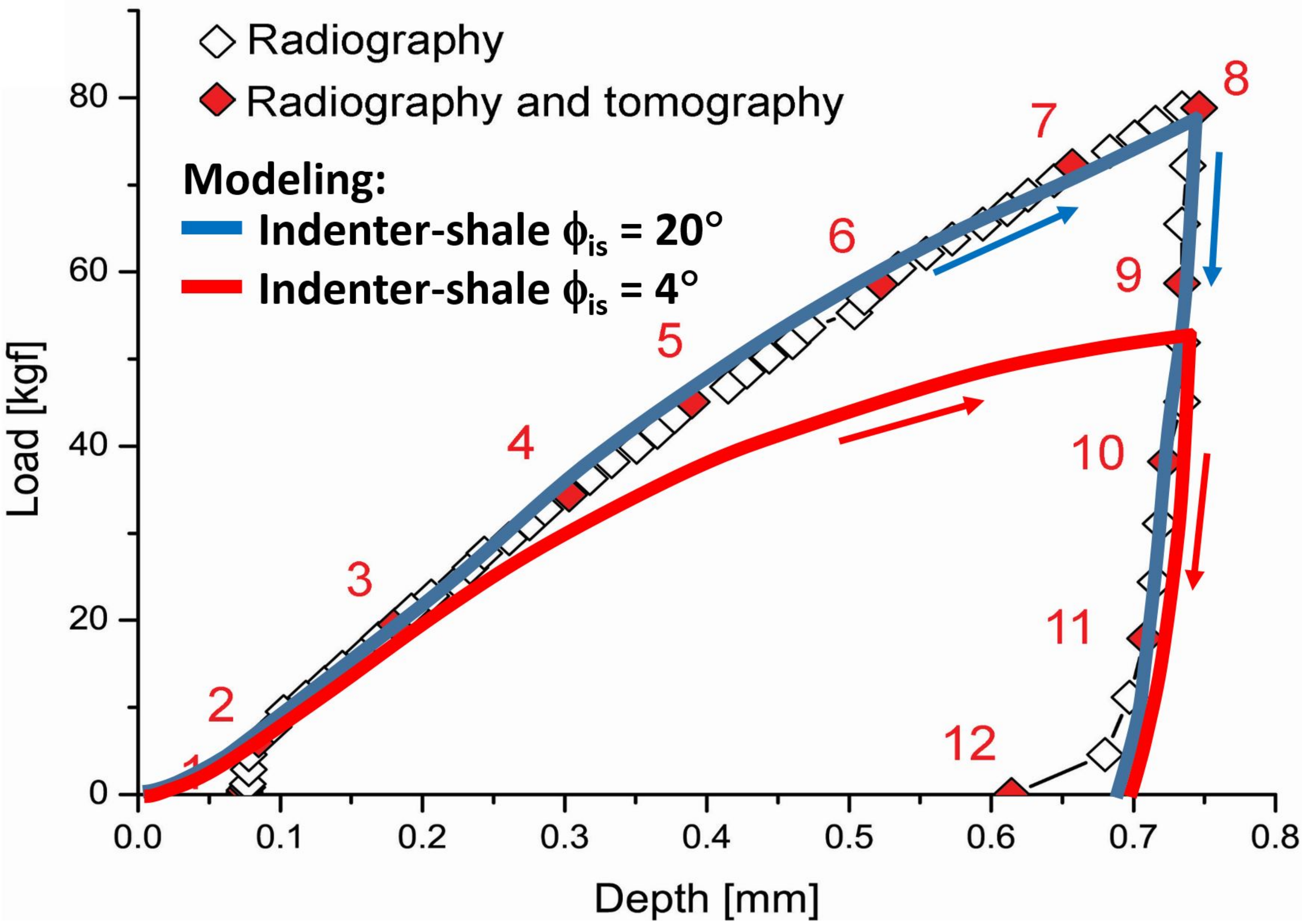

Radiography
Radiography and tomography
Modeling:
Indenter-shale ϕ_{is} = 20°
Indenter-shale ϕ_{is} = 4°
1
2
3
4
5
6
7
8
9
10
11
12
Load [kgf]
Depth [mm]
0
20
40
60
80
0.0
0.1
0.2
0.3
0.4
0.5
0.6
0.7
0.8

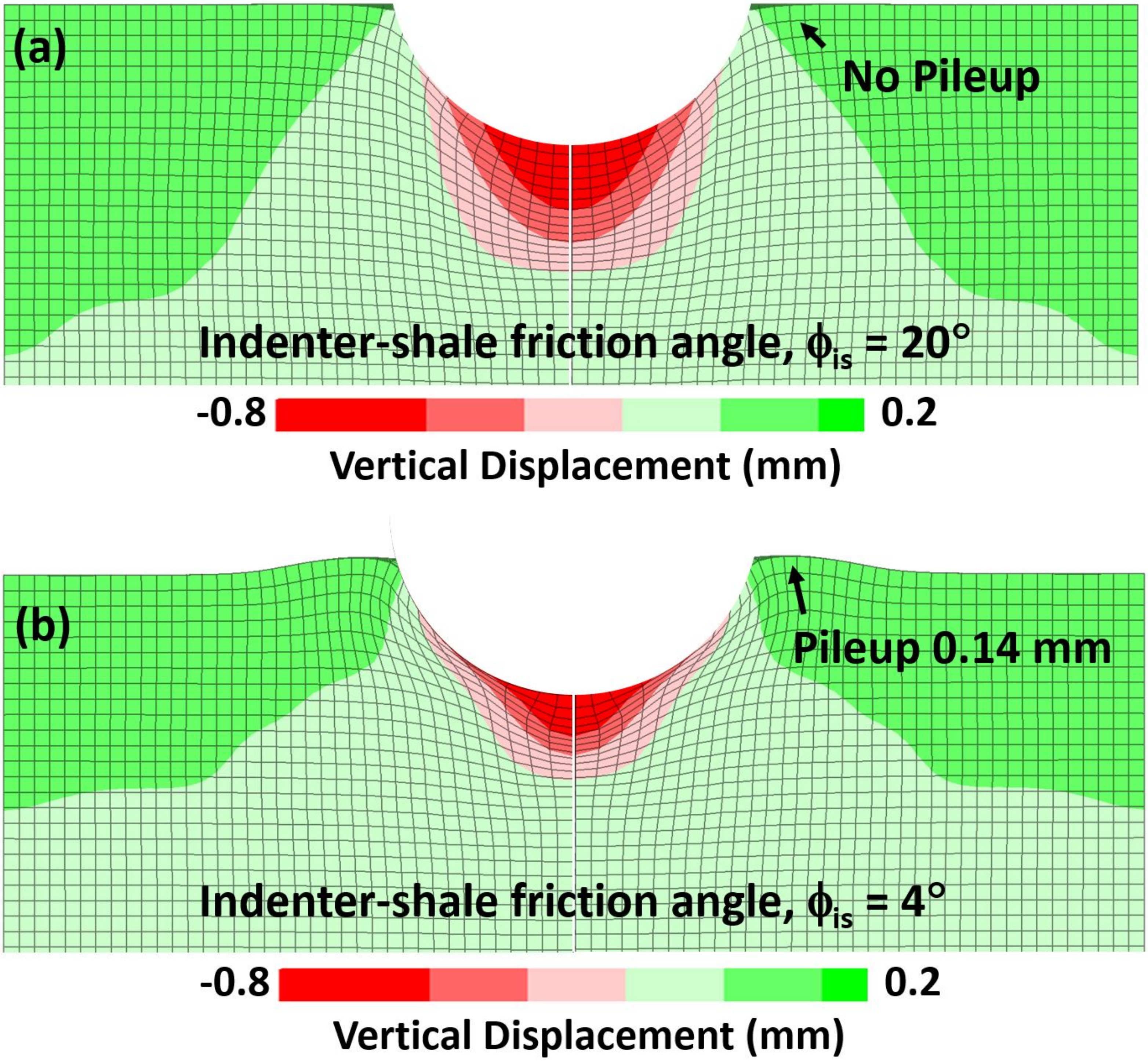

(a)
No Pileup
Indenter-shale friction angle, ϕ_{is} = 20°
-0.8
0.2
Vertical Displacement (mm)
(b)
Pileup 0.14 mm
Indenter-shale friction angle, ϕ_{is} = 4°
-0.8
0.2
Vertical Displacement (mm)

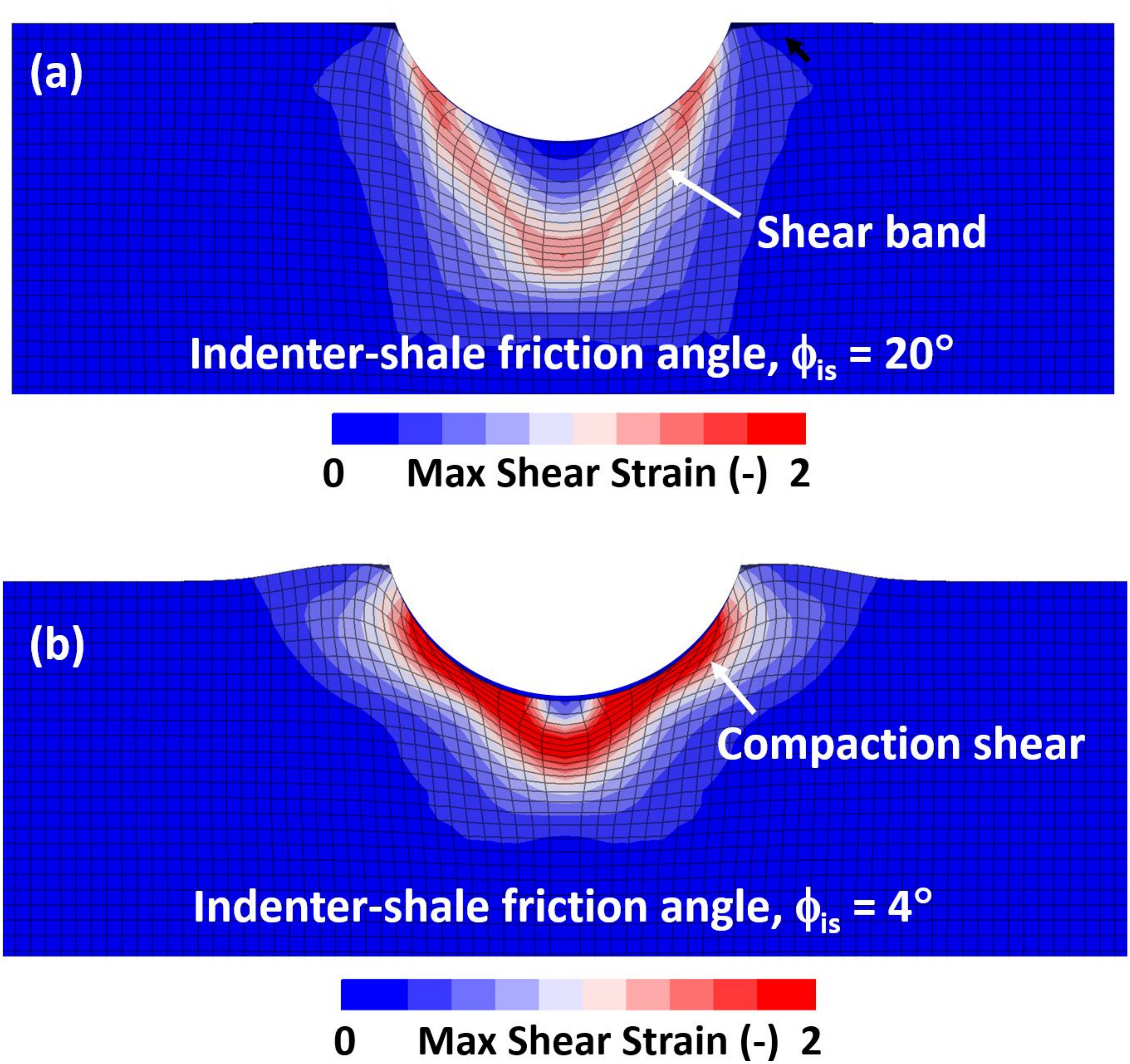
(a)
Shear band
Indenter-shale friction angle, ϕ_{is} = 20°
0 Max Shear Strain (-) 2
(b)
Compaction shear
Indenter-shale friction angle, ϕ_{is} = 4°
0 Max Shear Strain (-) 2

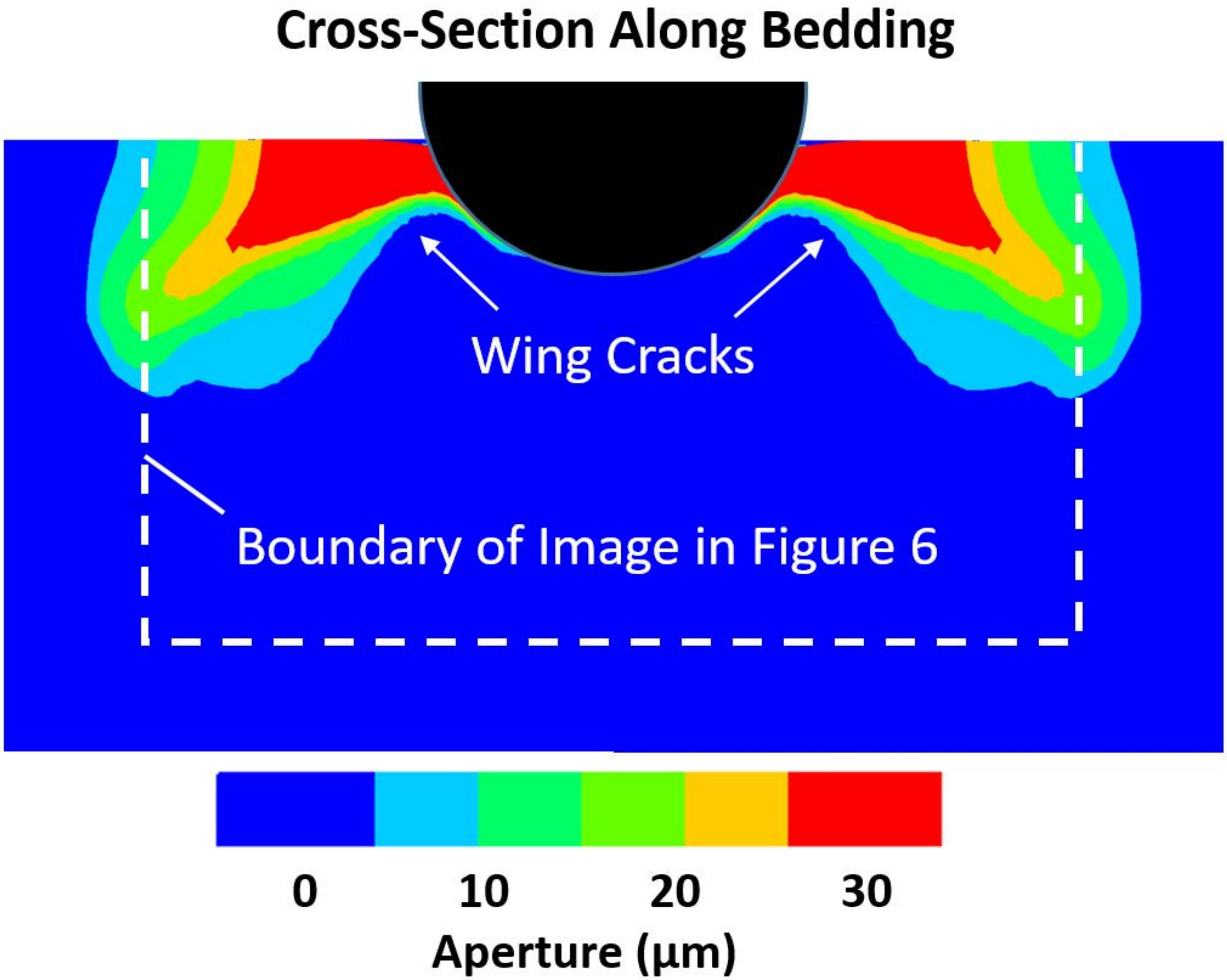
Cross-Section Along Bedding
Wing Cracks
Boundary of Image in Figure 6
0
10
20
30
Aperture (µm)